EBSD, XRD and SRS characterization of a casting Al-7wt%Si alloy processed by equal channel angular extrusion: Dislocation density evaluation

Zahra Zribi, Hassan Houcin Ktari, Frédéric Herbst, Virgil Optasanu, Nabil Njah

https://doi.org/10.1016/j.matchar.2019.04.044

EBSD, XRD and SRS characterization of a casting Al-7wt%Si alloy processed by equal channel angular extrusion: Dislocation density evaluation.

Zahra Zribi[1], Hassan Houcin Ktari[1], Frédéric Herbst[2], Virgil Optasanu[2], Nabil Njah[1]*

[1]GEOGLOB Lab, Sfax Faculty of Sciences, University of Sfax, PB 1171 (3000) Sfax (Tunisia).

[2] ICB, UMR 6303 CNRS, Université de Bourgogne Franche Comté, 9 av. Alain Savary, 21078 Dijon Cedex,France

*Corresponding author: Nabil.Njah@fss.rnu.tn

Abstract

Aluminum-silicon (Al-Si) alloys of high silicon contents are composite materials; they are used whenever high casting properties are required. They are slightly ductile below 8wt%Si. An increase in ductility can be obtained by refining Si-crystals in elaboration or by a further hot working. In the present work, an Al-7wt%Si alloy was processed by Equal Channel Angular Extrusion (ECAE) at temperatures 20°C and 160°C up to three passes. The die was formed by two cylindrical channels intersecting at an angle $\Phi = 110°$ without curvature at the outer corner ($\Psi=0$). EBSD observations, X ray diffraction (XRD) and Strain Rate Sensitivity (SRS) were used to characterize the microstructure and the mechanical properties. The activation volume of deformation is decreased by ECAE and a high level of strain was introduced at both temperatures. The remaining dislocation densities calculated from EBSD, XRD and SRS experiments are quite different. This was explained by the sensitivities of the methods to the free surface effect.

Key words: Aluminum alloys, ECAE; EBSD; Activation volume; Dislocation density

1. Introduction

Aluminum-Silicon alloys are widely used in casting [1]. Without copper alloying, they exhibit a medium strength but a good corrosion resistance. They are used whenever excellent castability is preferred to good mechanical properties like in complex shaped molds. In fact, silicon allows a high fluidity and a low shrinkage in solidification which are the main properties considered in castings.

Even though the maximum casting properties are obtained at the eutectic composition, they become suitable since 7wt% Si [2]. Furthermore, silicon has a low density which is an advantage in reducing the weight of the alloy. The high hardness of silicon particles is exploited for wear resistance [3].

As cast, the microstructure is formed by dendrites of a FCC solid solution and eutectic zones (for convenience, solid solution will be designated shortly by aluminum below). The eutectic silicon is virtually pure silicon which crystals have complex shapes and most of them are three dimensionally linked; this promotes crack propagation along these crystals and brittleness [4, 5]. The ductility can be improved by refining silicon crystals through the introduction of nucleation promoters like Na, P, Bi in liquid or by the high cooling speed in metallic molds. In alloys below 8% Si, the aluminum dendrites dominate and the mechanical properties are affected by the cell sizes and the dendrite arm spacing. For this reason, refinement of the aluminum grains in such alloys has taken only a weak importance [6].

ECAE has been widely used for microstructure refinement of metals by introducing high amount of plastic deformation [7, 8]. An idealized description of the procedure assumes that deformation consists in pure shearing [9]. ECAE was limited roughly to ductile alloys mainly single phased ones; in precipitation hardened alloys, it was shown to fracture large precipitates like θ- Al_2Cu in Al-Cu-Mg alloys [10]. For casting alloys, ECAE was rarely applied because of a dramatic brittleness [4, 6]. Previous works [3] have shown that matrix grains in Al-7wt% Si alloy can be refined up to 200nm by ECAE whereas silicon crystal size can be lowered up to 1-2 µm. The refinement seems to be more pronounced than that in pure Al-Si solid solution or in dilute Al-alloys [4]. At high temperatures, ECAE leads to coarser grain sizes with relatively low strain levels [11-13].

The mechanical property investigations of casting alloys were mostly limited to conventional tests [6]. However, the elementary deformation mechanisms, mainly those relative to activation volume, have not been very attractive. In the present work, the effects of ECAE on the microstructure and on the mechanical properties of a casting Al-7wt%Si were investigated. We focused on the quantification of the dislocation density introduced using XRD, EBSD and SRS techniques. We will summarize below the theoretical backgrounds considered for this purpose.

The presence of a high dislocation density leads to a local lattice strain affecting the peak shape in diffraction experiments [14]. The peak profile can be fitted by a pseudo-Voigt function which has been widely used in structural refinements [15], which is a convolution of the size (Cauchy) and strain (Gaussian) components. The breadths of each component are given by [16, 17]:

$$\beta_D = \frac{\lambda}{D\cos\theta} \quad (1a)$$

$$\beta_\xi = 2\xi \tan\theta \quad (1b)$$

Where λ is the radiation wavelength, θ is the diffraction angle, D is the crystallite size and ξ is the root mean square (rms) strain. An average value of the dislocation density ρ_X can be calculated by using the equation [18]:

$$\rho_X = \frac{2\sqrt{3}\xi}{D.b} \quad (2)$$

where b is the magnitude of the Burgers vector of dislocations.

Dislocations can be classified in two categories: The Statistically Stored Dislocations (SSDs) which do not create long range lattice deformation (the sum of their Burgers Vector is zero) [19] and the Geometrically Necessary Dislocations (GNDs) which allow the accommodation of the lattice curvature [20, 21]. If the Stacking Fault Energy (SFE) is sufficiently high, like in Al or Ni alloys, the GNDs are able to change their slip plane so that three-dimensional (3D) configurations are obtained; among others, high angle boundaries with high dislocation densities are obtained [22]. The relatively recent imaging techniques based on the local perturbations of diffraction patterns are powerful tools for the microstructure investigations. Thus, EBSD in Scanning Electron Microscopy (SEM) and orientation imaging ASTAR in Transmission Electron Microscopy (TEM) are commonly used for grain structure investigations [6, 23 – 25]. In both cases, the diffraction pattern can be calculated pixel by pixel revealing very locally changes in orientation. In EBSD, the GND density ρ_{GND} at each measurement point can be calculated from an averaging of the local disorientation θ_{ij} over the neighboring pixels j located at a fixed distance from the considered pixel i. The GND density is given by [26-30]:

$$\rho_{GND} = \frac{\alpha<\theta_{ij}>}{b.x} \quad (3)$$

Where α is a constant which depends on the nature of dislocations edge or screw, a value $\alpha = 3$ was proposed [31]; $< \theta_{ij} >$ is the average value of θ_{ij}, b is the magnitude of the Burgers vector of dislocations and x is the distance along which $< \theta_{ij} >$ is calculated. If the calculations take into account the peripheral pixels of the kernel, $< \theta_{ij} >$ represents the Kernel Average Misorientation angle (KAM) proposed by all EBSD data processing software packages; equation (3) is then replaced by:

$$\rho_{GND} = \alpha \frac{KAM}{b.R} \qquad (4)$$

KAM values are given by the EBSD software and *R* is the kernel size taking into account the neighbor order considered in the KAM mapping.

When the microstructure scale is reduced to few hundreds of nanometers, which is the case in severely deformed alloys, the deformation thermodynamics is affected so that a dependence of the flow stress on the strain rate can be observed. The strain rate sensitivity (SRS) parameter m is given by:

$$m = \frac{d \ln \sigma}{d \ln \dot{\varepsilon}} \qquad (5)$$

where σ is the flow stress and $\dot{\varepsilon}$ is the strain rate. In thermal activation analysis, the physical parameter directly related to the SRS is the activation volume *V**; it means the unit volume of the crystal directly affected by dislocation movements [32] or the region swept by a dislocation and can be expressed by [33,34]

$$V^* = -\frac{\partial \Delta G}{\partial \tau^*} = k_B T \left(\frac{\partial \ln \frac{\dot{\gamma}}{\dot{\gamma}_0}}{\partial \tau *} \right)_{T,G,S} \qquad (6)$$

where ΔG is the free enthalpy variation, $\dot{\gamma}$ is the shear strain rate, $\tau^* = \tau - \tau_G$, is the shear stress responsible of dislocation motion, τ is the applied shear stress (experimental), τ_G is the athermal component due to the intrinsic resistance of the lattice to flow, k_B is the Boltzmann constant and *T* is the temperature. Only τ* is strain rate dependent. Writing that $\dot{\gamma}/\dot{\gamma}_0 = \dot{\varepsilon}/\dot{\varepsilon}o$ and $\sigma^* = M.\tau^*$, equation (6) becomes:

$$V^* = M k_B T \left(\frac{\partial \ln \frac{\dot{\varepsilon}}{\dot{\varepsilon}_0}}{\partial \sigma^*} \right)_{T,G,S} \qquad (7)$$

M is the Taylor factor linking the stress in polycrystalline materials to the shear stress. A value $M \simeq 3$ is generally adopted both in coarse-grained and fine-grained materials [33]. Since $\dot{\gamma}_0$ and then $\dot{\varepsilon_0}$ are not accessible, an apparent activation volume is rather adopted; it is defined by:

$$V^*_{app} = M\, k_B T \left(\frac{\partial \ln \dot{\varepsilon}}{\partial \sigma^*} \right)_{T,G,S} \qquad (8)$$

and for macroscopic variations, equation (8) can be replaced by:

$$V_{app}^{*} = M\, k_B T \left(\frac{\Delta \ln \dot{\varepsilon}}{\Delta \sigma^{*}}\right)_{T,G,S} \qquad (9)$$

$\Delta\sigma^{*}$ is related to the experimental stress variation $\Delta\sigma$ by $\Delta\sigma^{*} = \Delta\sigma\,(1+K/Y)$, with $K \simeq \theta = d\sigma/d\varepsilon$ with is the strain hardening and Y is the modulus of specimen-machine assembly [34].

When the obstacles to slip are mainly the forest dislocations, $V^{*} = b.\lambda_{sp}.l^{*}$ where λ_{sp} is the average effective barrier width, $\lambda_{sp} \simeq b$ [35, 36], l^{*} is the average dislocation spacing which can be expressed by $l^{*} = \rho^{-1/2}$ [35]. Thus, the total dislocation density can be expressed by:

$$\rho = \left(\frac{V^{*}}{b^{2}}\right)^{-2} \qquad (10)$$

2. Material and Methods

The alloy of the present investigation is an Al-7wt%Si alloy. An ingot was prepared by melting together weighed quantities of pure aluminum and an Al-13wt%Si master alloy. To reduce porosity after solidification, small quantities of tin (Sn) and antimony (Sb) were added but the Si/(Al+Si) ratio was fixed to 7wt%. The alloy composition is given in table 1; it was fixed in elaboration and verified by X Ray Fluorescence (XRF). Owing to their higher densities (7.28 g/cm^3 for Sn and 6.67 g/cm^3 for Sb) as compared to that of Al (2.70 g/cm^3) and silicon (2.34 g/cm^3), their volume fraction in the alloy remains very small. The alloy was melt in crucible furnace and cast in steel mold. For ECAE, cylindrical specimens of 10mm diameter and 70mm height were wire-machined. ECAE experiments were performed via route A [37] at temperatures of 20°C and 160°C. The die was machined from tool steel. The channels intersect according to the angles $\Phi = 110°$ and $\Psi = 0°$ [38]; this geometry leads to an equivalent strain after each number of passes through the die $\varepsilon_N = 0.7N$ [39]. For the high temperature experiments, the specimen is kept for one minute in the channel before deformation to reach the chosen temperature. Specimens for EBSD were cut from the central part of the extruded specimens; they were mechanically polished up to 1 µm diamond powder then super-finished with 50 nm colloidal silica suspension. The observations were performed on X and Y planes [37].

Si	Sn	Sb	Al
6.8	2.7	0.4	90.1

Table 1: Alloy composition (wt%)

SEM and EBSD observations were performed using a JEOL JSM 7600F SE microscope equiped with the EBSD TSL EDAX OIM system. The grains were analyzed directly from the OIM images using pixel-to-pixel measurements. A critical misorientation angle of 15° was considered to differentiate low-angle grain boundaries (LAGBs) from high-angle grain boundaries (HAGBs).

In the present study, the KAM was explored to calculate the dislocation density ρ_{GND} by using equation (4). It has been shown [40] that for phase quantification, the optimum kernel size is close to the sub-structure size. In the present investigation, silicon crystals in eutectic zones are close to 5 µm and the space between them is of the same order. The step used for recording the KAM images was 1.5 µm for large images and 100 nm for close-up images of regions around the rigid Si grains. The KAM images were recorded using the 3rd neighbor, which corresponds to a kernel size of 4.5 µm and 0.3 nm respectively.

X Ray Diffraction (XRD) experiments were focused on the calculations of the dislocation density after ECAP. Diffraction patterns were recorded on the X plane at room temperature using a Bruker D8 diffractometer in the theta/theta mode and using Cu(Kα) radiation. The step size was 0.015° in theta and the counting time was 2s. Each peak was fitted by a pseudo-Voigt function. After subtracting the Kα_2 and instrument contributions, the extracted components i.e. the Cauchy (β_C) and Gaussian (β_G) integral breadths were used to calculate the coherency length D and the rms-strain ξ by using equations (1). It should be noted that the (200) peak is partially screened by a silicon peak and it was not taken into account. The same specimens were used in XRD and EBSD experiments so a comparison between the results obtained by the two methods is possible.

Strain rate jump tests in compression were performed at room temperature on cylindrical specimens of 12 mm height and 10mm diameter machined in the ECAE direction. Tests were performed using Tinius Olsen machine 50 KS piloted with Qmat software. Strain rates used ranged between 3.10^{-5} and 10^{-2} s^{-1}. The machine stiffness is first measured by recording force-displacement during platen to platen contact experiment. In order to minimize the friction effect, the contact surfaces of the specimens were coated with a lubricant containing colloidal MoS_2 suspension.

3. Results

Figure 1 shows the IPF of the alloy before ECAE. The microstructure after casting is formed by Al-dendrites and eutectic zones (Fig 1a). Many orientations can be revealed even in the same dendrite. The selected zone was highlighted by various imaging techniques in figure 1a-f. An intergranular region was repaired to check the complementarity of the various imaging techniques. BSE image (Fig. 1b) and silicon EDX cartography (Fig. 1c) show that most of silicon is located in the interdendritic zones, i.e. the eutectic zone. The eutectic fraction, as determined using the straight-line method, is close to 50%, which is consistent with the silicon content in the alloy. Since both Al and Si lattices are cubic (FCC and Diamond Cubic respectively), their IPF are recorded

simultaneously and the microstructure of silicon should merge with that of aluminum. However, reliable methods have been developed to identify phases of the same crystallography such as image quality (IQ) [41-46], since it is based on the degree of lattice imperfection. In the present case, it is easy to separate metallic zones exhibiting high dislocation density (α- aluminum) from brittle silicon. The IPF, IQ and KAM images (Fig 1d-f) show that silicon exhibits a granular structure close to 10 µm in size. These figures show also that the starting grain size of aluminum after casting is close to 100 µm. As it was presented above, KAM values are closely related to GND density. The color code used in Figure 1f shows that silicon grains are free of dislocations (blue color) whereas aluminum grains contain a relatively high dislocation density (green-yellow).

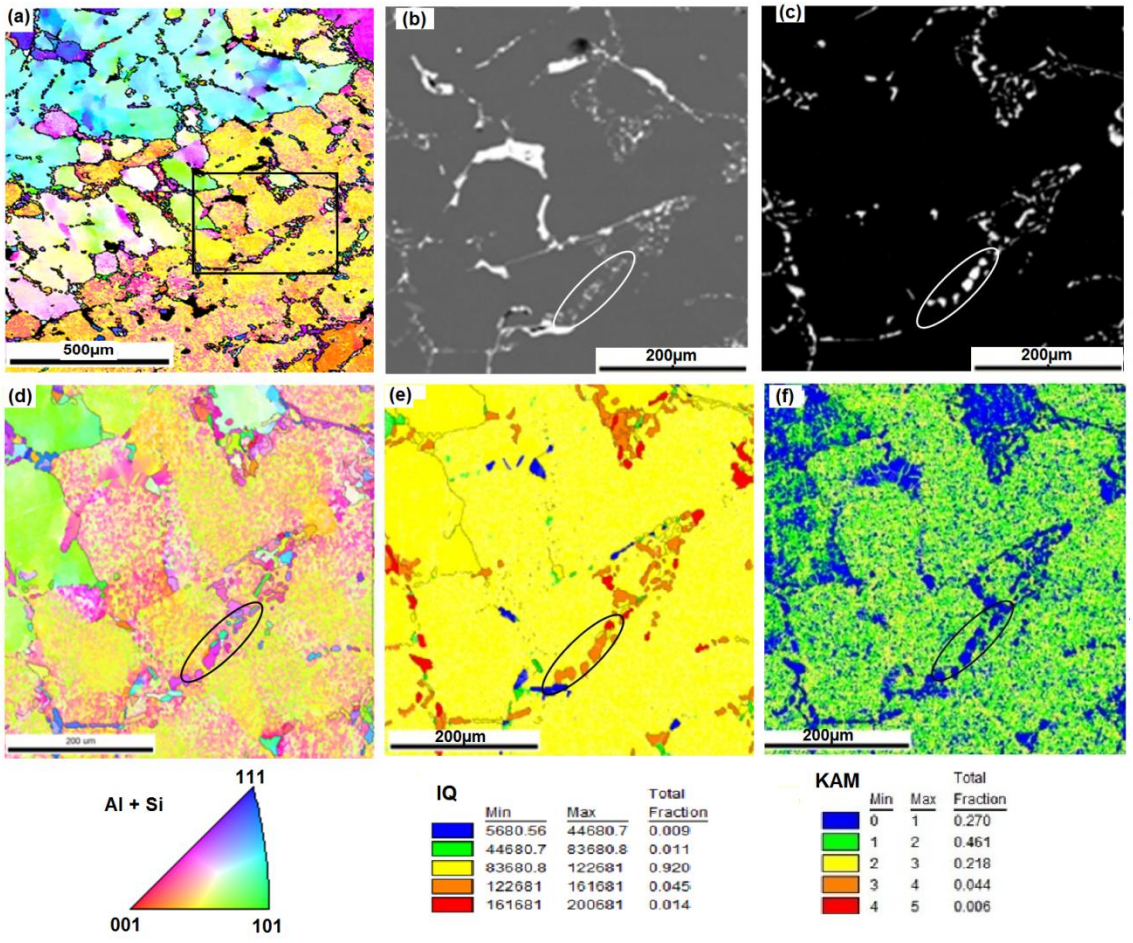

Figure 1 (a): Microstructure of the as cast Al-7wt%Si alloy: Inverse pole figure (IPF) [001]. (b-f): Magnifications of the selected zone. (b) BSE image; (c) Silicon cartography (Si Kα); (d) IPF [001]; (e) IQ image; (f) KAM image. Color codes used in IPF, IQ and KAM mapping are given.

The IQ image of Figure 1e confirms the lower coherence of metallic grains (yellow) as compared to silicon ones in the intergranular region (red-brown).

Figure 2 presents the IPF and KAM images of the alloy deformed for N=3 at 20°C and 160°C recorded on the X plane. Many selections were made to link the microstructures obtained by the various imaging techniques. Rectangles show eutectic colonies while ellipses and star-shaped symbols present aluminum grains. The grain boundaries are well revealed. In specimen deformed at 20 °C, an elongation of aluminum grains is observed so that the pre-existing grain boundaries cannot be clearly revealed (Fig. 2a). When ECAE is realized at 160 °C, the aluminum grains remain almost equiaxe (Fig. 2d). At two temperatures, silicon crystals seem to have the same shape and size (15 µm) as before ECAE. From the color codes of the KAM images, converted to GND densities using equation 4, we note that a high dislocation density exists solely within aluminum grains whereas silicon crystals appear to be free of dislocations (Fig 2b and e). The magnifications c and f show that a high GND density is stored when ECAE is performed at 20°C. The images recorded on the Y plane for N=3 at 20°C (Fig 3) show a clearer elongation of the aluminum grains.

IPF and KAM images of a eutectic zone are given in figure 4 for samples after ECAE (N=3) at both temperatures. IPF show that aluminum grains are strongly compressed around a large silicon crystal (arrowed area, figure 4a); this causes a splitting of the latter (double arrows). In KAM (Fig. 4c), blue zones (KAM=0°-1° of misalignment between neighbors) are mainly relative to undeformed phase (silicon) since it is expected to be free of dislocations. At 160°C, the compression of aluminum grains is less pronounced indicating an easier flow (Fig. 4b and d).

To understand the changes in the microstructure observed after ECAE, XRD and SRS in compression experiments were also performed. The evolution of the line profile of the normalized (111) peak relative to aluminum-matrix is shown in figure 5. We note that the experimental points are well fitted by a pseudo-Voigt function. A broadening of the peaks is observed at both temperatures but it is more pronounced at 20 °C. XRD experiments were focused on the calculations of dislocation density ρ_X after ECAE. In such alloy of high stacking fault energy, the broadening of the XRD peaks (Fig. 5) is due to a reduction in the crystallite size D and to an increase in the root mean square strain ξ. D and ξ were calculated from the broadening of several peaks by using equations (1). The average values of D and ξ were used to calculate ρ_X by using equation (2). Figure 6 shows the evolution of D and ξ against the number of passes N. A decrease in D and an increase in ξ are observed since the first pass through the die.

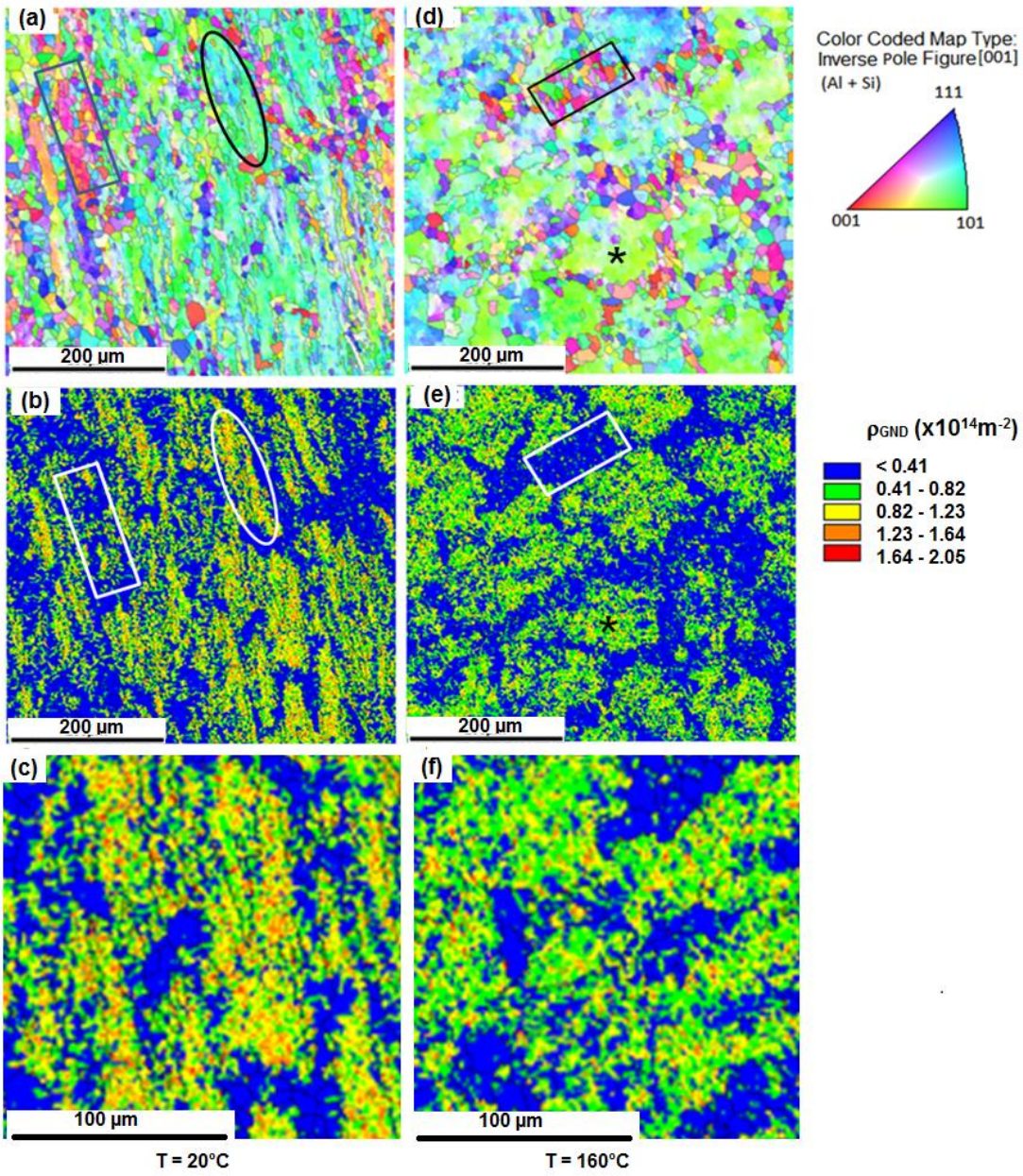

Figure 2: Microstructures of the as cast Al-7wt%Si alloy after ECAE for N = 3 at 20°C (a-c) and 160°C (d-f). (a, d): IPF (same color codes as figure 1); (b, e): the corresponding GND dislocation density mapping as calculated from KAM images (c, d), equation (4); Ellipses and asterisks denote aluminum; rectangles denote eutectic zones. (c) and (f): Magnifications of (b) and (e) respectively.

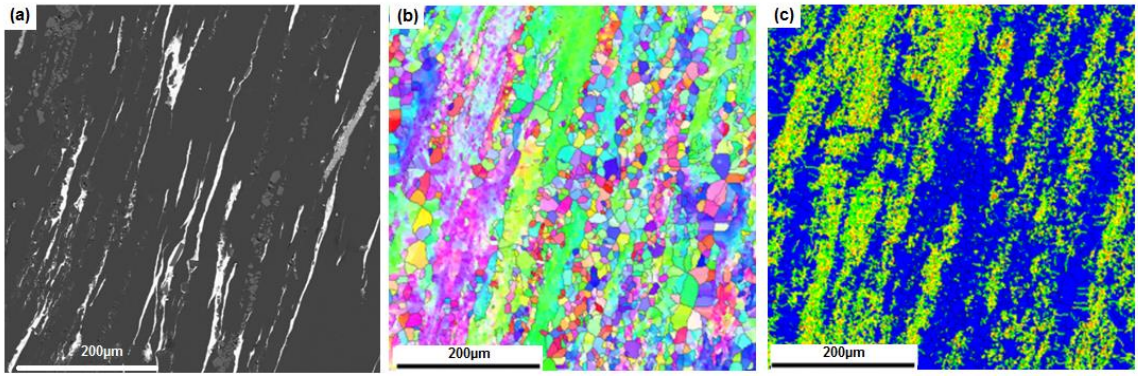

Figure 3: Microstructure of the as cast Al-7wt%Si alloy after ECAE for N = 3 at 20°C recorded on the Y plane. (a): BSE image, (b): IPF image and (c): KAM image. Same color codes as in figure 1.

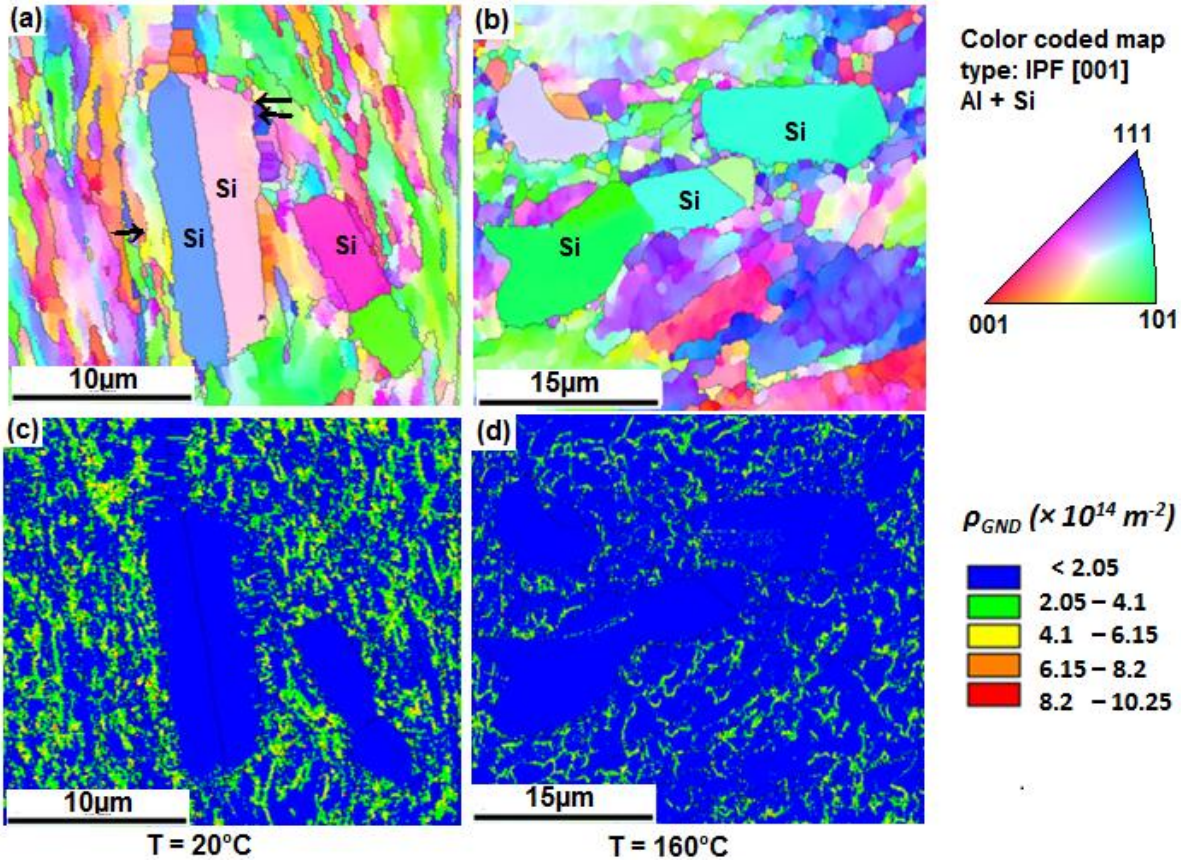

Figure 4: Aluminum grain morphology in the Al-7wt%Si alloy in the vicinity of silicon crystals after ECAE (N=3) at temperatures 20°C and 160°C. (a, c): IPF images (same color codes as figure 1); (b, d): GND dislocation density mapping as calculated from KAM images (equation (4).

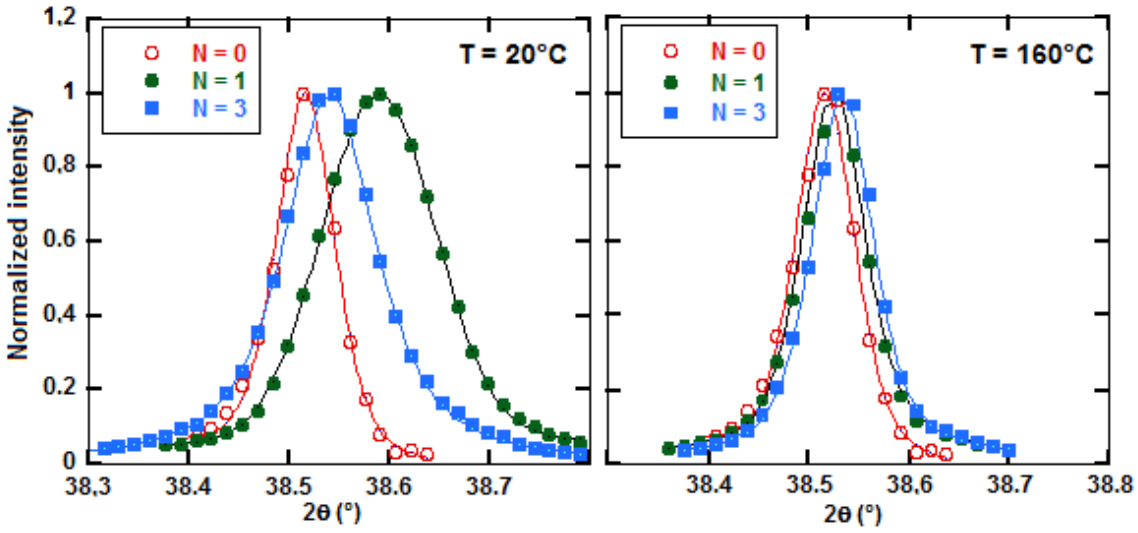

Figure 5: Profiles of the (111) aluminum peak in the as cast Al-7wt%Si alloy before and after ECAE at temperatures 20°C and 160°C fitted by pseudo-Voight functions (normalized intensities).

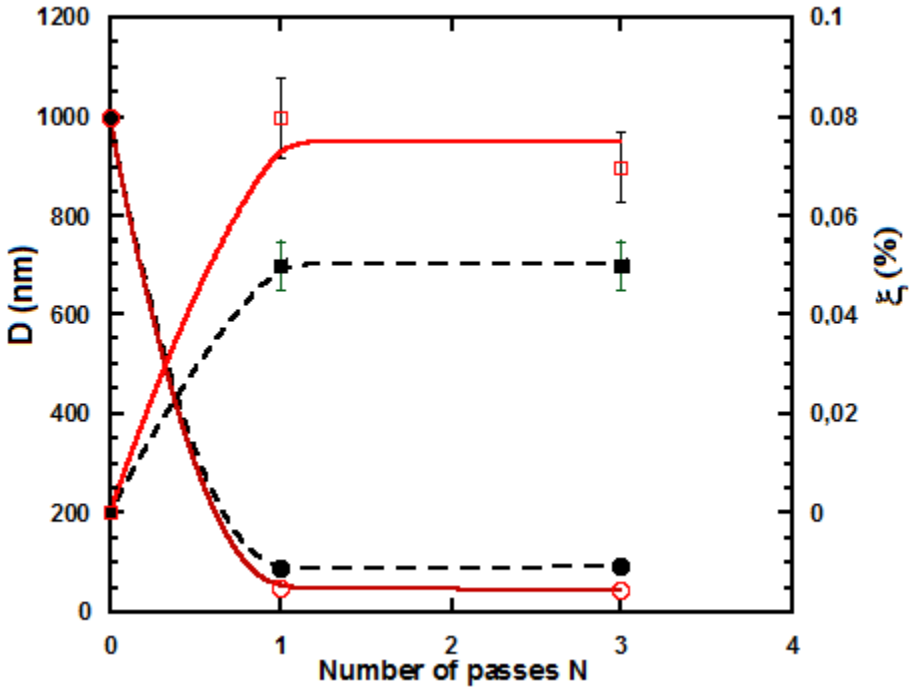

Figure 6: Crystallite size D (circles) and rms strain ξ (squares) of the as cast Al-7wt%Si alloy after ECAE at temperatures 20°C (open marks) and 160°C (full marks).

SRJ curves in compression are given Figure 7. We note that the flow stress is increased by ECAE since the first pass, indicating a whole strengthening of the material. Figure 8 shows the 0.2% flow stress as a function of number of passes. At 20 °C, a saturation value is achieved since the first pass through the die whereas at 160 °C an increase is observed up to N=3. The curves of figure 7 show also that in deformed alloys, the flow stress is more sensitive to strain rate.

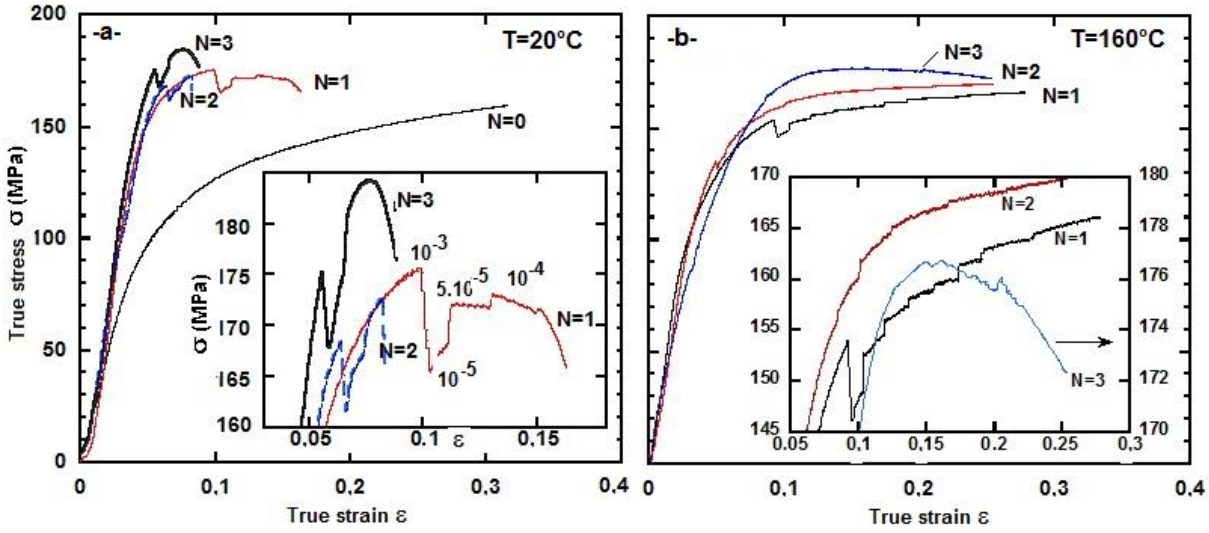

Figure 7: Strain rate jump curves in compression of the as cast Al-7wt%Si alloy before and after ECAE at temperatures 20°C and 160°C. Plastic part of the ECAE processed specimens was magnified. Note the scale difference on the stress axis in the magnification of (b).

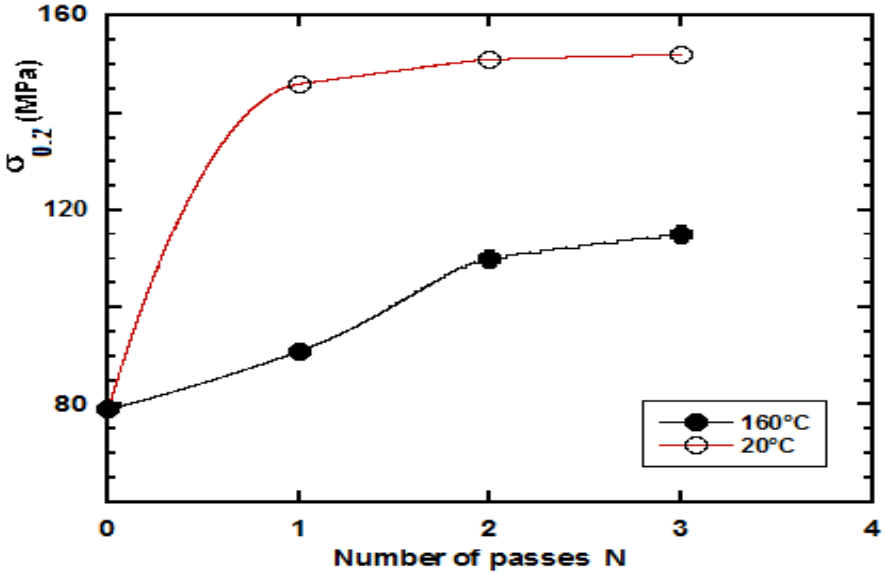

Figure 8: Effects of ECAE at 20°C and 160°C on the 0.2% flow stress of the as cast Al-7wt%Si alloy.

4. Discussion

The GND densities in the Al grains were calculated from the KAM mapping. For this purpose, the eutectic colonies and Si grains were excluded from the images and an average value was computed by taking into account the remaining misorientation fractions within aluminum grains. The calculated values are given in table 2. On the close-up images of the eutectic zones, the mean values obtained in the aluminum part were rather 6.1 $10^{14}m^{-2}$ and 4.3 $10^{14}m^{-2}$ at 20°C and 160°C respectively; slightly higher than those of the aluminum grains. Since the whole plastic deformation is devoted to aluminum, the difference between the values arises from an eventual dislocation pile-up in the vicinity of the rigid silicon crystals. Also, the smaller fraction of the Al volume in the eutectic zone as compared with that in the pro-eutectic region, with sensibly higher proportion of grain boundaries, is conductive to a higher dislocation density.

A decrease in D and an increase in ξ are observed after ECAE at both temperatures (figure 6). Furthermore, the difference between D values at two temperatures for N=3 is close to 14% whereas the difference between ξ is close to 50%; that means that a slight relaxation occurred at high temperature without a significant increase in crystallite size. The values of the dislocation density ρ obtained are given in table 2.

The increase in the 0.2% flow stress $\sigma_{0.2}$when ECAE is performed at 160 °C (Fig. 7, 8) indicates a continuous storage of deformation at this temperature; this is due to a simultaneous recovery of the microstructure. Furthermore, the lower values of $\sigma_{0.2}$ are accompanied by a significant strain hardening mainly for N=1 and N=2 (the slopes of plastic part of the curves in figure 7b are higher). The sensitivity of the flow stress to the strain rate after ECAE (Fig. 7) indicates that the activation volume of deformation has accessible values. An apparent activation volume after each number of passes was calculated by using equation (9). In the present case, for N=0, K/Y was calculated to be 0.038 so that $\Delta\sigma \simeq \Delta\sigma^*$. The value of σ at a given strain rate was determined from the intercept of the extrapolation lines of the considered part and the elastic part of the curve. The apparent activation volume V* normalized to b^3 are plotted in figure 9 as a function of N. At both temperatures, measurable values of V* were obtained since N=1. For N=3, the reached values are 125 b^3 and 210 b^3 at 20 °C and 160 °C respectively.

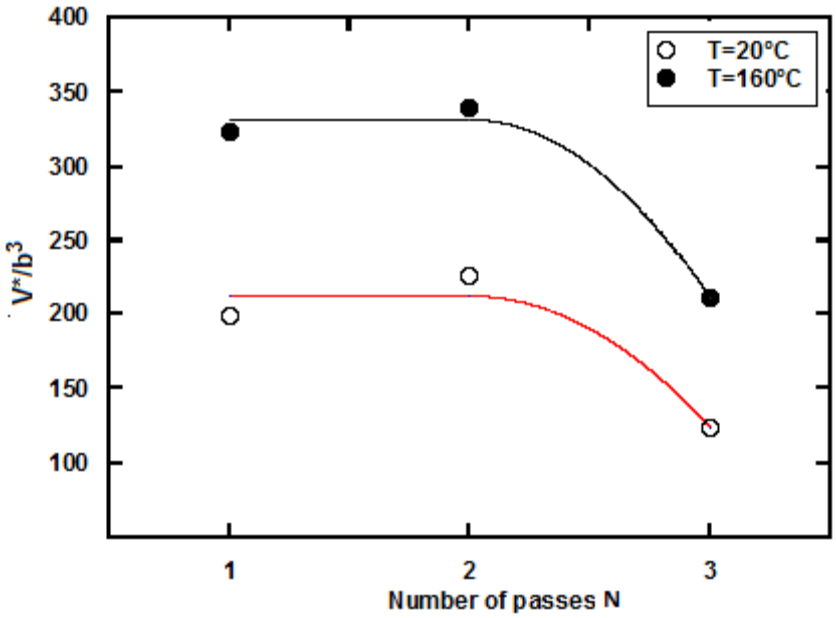

Figure 9: Normalized apparent activation volume in the as cast Al-7wt%Si alloy after ECAE at temperatures 20°C and 160°C.

The dislocation density as calculated from different experiments is given in table 2.

ECAE temperatu	Number of passes	KAM: $\rho_{GND} = \alpha \frac{KAM}{bx}$	XRD: $\rho x = \frac{2\sqrt{3}\xi}{D.b}$	SRS: $\rho = \left(\frac{V^*}{b^2}\right)^{-2}$
20°C	1	0.8	2	2.9
	3	0.8	1.9	7.5 (2.3 for N=2)
160°C	1	0.8	0.7	1.1
	3	0.7	0.7	2.6 (1 for N=2)

Table 2: Dislocation densities obtained from XRD, EBSD and SRS experiments (x $10^{14}m^{-2}$).

The figures of table 2 show that, saturation values of ρ are obtained since N=1. The values obtained from SRS are in good agreement with the value 4.5 $10^{14}m^{-2}$ obtained by Cardoso et al. [6] from mechanical tests in as cast Al-10 wt% Si after ECAE at room temperature. Physically, a direct comparison of the values obtained from different experiments is quite subjective since the three methods suffer from many limitations: ρ_{GND} is calculated from KAM, depending on the Kernel radius chosen i.e. the scale of orientation variations. Furthermore, the estimation of the dislocation density

in EBSD is sensitive to the noise and the method is able to estimate only a part of the noise, which may result in too much high values of ρ_{GND}. On the other hand, regarding the step size (or the kernel size) used in this study, the GND should correspond to misorientations quantified within sub-boundaries. The dislocation densities obtained from XRD aluminum peaks or SRS represent an average between the eutectic and the aluminum zones. Here, GND contribute by a high proportion in peak profiles or in the mechanical response but the wide area explored simultaneously in both methods leads rather to an average value.

Even though all the values are of the same order of magnitude, it is clear that $\rho_{GND} < \rho_X < \rho_{SRS}$; this can be explained by the sensitivity of each techniques on the surface effects. In fact, dislocation dynamics simulations show that there is a relaxation of the dislocation structure near the free surface of the specimen that extends approximately 65nm into the specimen [47]. Thus, EBSD which information volume extends only 10-20nm into the specimen [48-51], is more sensitive to the surface relaxation than XRD where the explored thickness reaches several microns [47]. On the other hand, when carefully smoothed, EBSD can distinguish between cells and random dislocations whereas XRD provides only an average value of ρ. The effects on the mechanical properties can be neglected regarding the much higher volume investigated.

Conclusion

Al-Si alloys of high Si content are widely used in casting. Without additions, the coarse silicon crystals lead to poor mechanical properties. Many attempts have been made to refine the microstructure by mechanical working. In the present work, the microstructure and the mechanical properties of a casting Al-7wt%Si alloy after ECAE were investigated by using EBSD imaging, XRD and SRS experiments. ECAE was performed at 20 °C and 160 °C up to three passes. The microstructure is formed by aluminum solid solution and eutectic colonies in the grain boundaries. IPF images of Al matrix and Si crystals were recorded simultaneously due to the same cubic lattice but they were differentiated in IQ images. Plastic flow occurs in both pro-eutectic and eutectic aluminum. ECAE leads to a significant reduction in crystallite size and in the activation volume of deformation at two temperatures. Dislocation density ρ calculated from KAM, XRD and SRS experiments revealed a partial recovery at 160 °C. EBSD imaging shows that the dislocations concentrate counter the silicon crystals. The values of ρ are significantly different: $\rho_{EBSD} < \rho_X < \rho_{SRS}$. This has been explained by the sensitivity to the near surface relaxation of the material which is higher in EBSD. Furthermore, KAM imaging presents the big advantage of providing the spatial distribution of dislocations.

References

[1] S. Anand, T.S. Srivatsan, Y. Wu, E.J. Lavernia, Processing, microstructure and fracture behaviour of a spray atomized and deposited aluminium–silicon alloy, J. Mater. Sci. 32 (1997) 2835–2848.

[2] M. Colombié and coll., Matériaux Métalliques, DUNOD, Paris (2000) 455.

[3] W.X.Shi, B. Gao, G.F.Tu, S.W.Li, Effect of Nd on microstructure and wear resistance of hypereutectic Al–20%Si alloy, J. Alloy Compd 508 (2010) 480-485

[4] G. Urrutia, M.A. Muñoz-Morris, D.G. Morris, Contribution of microstructural parameters to strengthening in an ultrafine-grained Al–7% Si alloy processed by severe deformation, Acta Mater. 55 (2007) 1319.

[5] D.G. Morris, M.A. Muñoz-Morris, Refinement of second phase dispersions in iron aluminide intermetallics by high-temperature severe plastic deformation, Intermetallics 23 (2012) 169.

[6] K. Regina Cardoso, M. A. Muñoz-Morris, K. Valdés León, D. G. Morris, Room and high temperature ECAP processing of Al–10%Si alloy. Mat. Sci. Eng. A 587 (2013)387–396

[7] V.M. Segal, V.I. Reznikov, A.E. Dorbyshevskity, V.I. Kopylov, Plastic working of metals by simple shear, Russ. Metall. 1 (1981) 99.

[8] V.M. Segal, Slip line solutions, deformation mode and loading history during equal channel angular extrusion, Mater. Sci. Eng. A 345 (2003) 36.

[9] A.P. Zhilyaev, D.L. Swisher, K. Oh-ishi, T.G. Langdon, T.R. Mc Nelley, microtexture and microstructure evolution during processing of pure aluminum by repetitive ECAP, Mater. Sci. Eng. A 429 (2006) 137–148.

[10] H. H. Ktari, J. P. Couzinie, J. Bourgon, Y. Champion, N.Njah, Orientation imaging- ASTAR investigation of the grain and precipitatemorphology in Al-Cu-Mg alloy processed by Equal Channel Angular Pressing, J. Alloy Compd 647 (2015) 152-158.

[11] I. Gutierrez-Urrutia, M.A. Muñoz-Morris, I. Puertas, C. Luis, D.G. Morris, Influence of processing temperature and die angle on the grain microstructure produced by severe deformation of an Al–7% Si alloy, Mater. Sci. Eng. A 475 (2008) 268.

[12] L. Deng, X. Wang, J. Xia, J. Li, Effect of isothermal extrusion parameters on mechanical properties of Al–Si eutectic alloy, Mater. Sci. Eng. A 528 (2011) 6504.

[14] J.H. Jiang, A.-B. Ma, D. Song, D.H. Yang, J. Shi, K. Wang, L.Y. Zhang, J. Chen, Anticorrosion behavior of ultrafine-grained Al-26 wt% Si alloy fabricated by ECAP, J. Mater. Sci. 47 (2012) 7744.

[15] B. Jiang, N. Hou, S. Huang, G. Zhou, J. Hou, Z. Cao, H. Zhu, Structural studies of TiC1xOx solid solution by Rietveld refinement and first-principles calculations, J. Solid State Chem. 204 (2013) 1–8.

[16] T. Ungár, Dislocation densities, arrangements and character from X-ray diffraction experiments, Mater. Sci. Eng. A 309–310 (2001) 14

[17] H.P. Klug, L.E. Alexander, X-ray Diffraction Procedures, 2nd ed. John Willey & Sons, 1974. 662

[18] S.M. Dasharath, S. Mula, Microstructural evolution and mechanical properties of low SFE Cu-Al alloys processed by cryorolling followed by short-annealing, Mater Design 99 (2016) 552–564.

[19] D.A. Hughes, N. Hansen, D.J. Bammann, Geometrically necessary boundaries, incidental dislocation boundaries and geometrically necessary dislocations, Scripta Mater. 48 (2003) 147–153.

[20] J.F. Nye, Some geometrical relations in dislocated crystals, Acta Metall. 1 (1953) 153–162.

[21] M.F. Ashby, The deformation of plastically non-homogeneous materials, Philos. Mag. 21 (1970) 399–424.

[22] D. Kuhlmann-Wilsdorf, N. Hansen, Geometrically necessary, incidental and subgrainboundaries, Scr. MetallMater. 25 (1991) 1557–1562.

[13] T. Ungar, Microstructural parameters from X-ray diffraction peak broadening, Scripta Mater 51 (2004) 777-781.

[23] Hailin He, Youping Yia, Shiquan Huang, Yuxun Zhang, An improved process for grain refinement of large 2219 Al alloy rings and its influence on mechanical properties J. Materials Science & Technology 35 (2019) 55–63

[24] Shrivastava P, Tandon P, Microstructure and texture based analysis of forming behavior and deformation mechanism of AA1050 sheet during single point incremental forming, Journal of Materials Processing Tech. (2018), https://doi.org/10.1016/j.jmatprotec.2018.11.012

[25] Edgar F. Rauch, Joaquin Portillo, Stavros Nicolopoulos, Daniel Bultreys, Sergei Rouvimov and Peter Moeck, "Automated nanocrystal orientation and phase mapping in the transmission electron microscope on the basis of precession electron diffraction." Zeitschrift für Kristallographie International journal for structural, physical, and chemical aspects of crystalline materials 225.2-3 (2010): 103-109.

[26] D.P. Field, C.C. Merriman, N. Allain-Bonasso, F. Wagner, Quantification of dislocation structure heterogeneity in deformed polycrystals by EBSD, Modelling Simul. Mater. Sci. Eng. 20 (2012) 024007.

[27] C. Moussa, M. Bernacki, R. Besnard, N. Bozzolo, About quantitative EBSD analysis of deformation and recovery substructures in pure Tantalum, IOP Conference Series: Materials Science and Engineering, 89 (2015) 012038

[28] J. Jiang, T.B. Britton, A.J. Wilkinson, Measurement of geometrically necessary dislocation density with high resolution electron backscatter diffraction: Effects of detector binning and step size, Ultramicroscopy 125 (2013) 1–9.

[29] B. El-Dasher, B. Adams, A. Rollett, Experimental recovery of geometrically necessary dislocation density in polycrystals, Scripta Mater. 48 (2003) 141–145.

[30] M. Calcagnotto, D. Ponge, E. Demir, D. Raabe, Orientation gradients and geometrically necessary dislocations in ultrafine grained dual-phase steels studied by 2D and 3D EBSD, Mater. Sci.Eng. A 527 (2010) 2738–2746.

[31] P.J. Konijnenberg, S. Zaefferer, D. Raabe, Assessment of geometrically necessary dislocation levels derived by 3D EBSD, Acta Mater. 99 (2015) 402–414.

[32]S. Nemat-Nasser, Y.L. Li, Flow stress of fcc polycrystals with application to OFHC Cu, Acta Mater. 46 (1998) 565-577.

[38]V.M. Segal, Equal channel angular extrusion: from macromechanics to structure formation, Mater. Sci. Eng. A. 271 (1999) 322–333.

[33] L. Lu, R. Schwaiger, Z.W. Shan, M. Dao, K. Lu, S. Suresh, Nano-sized twins induce high rate sensitivity of flow stress in pure copper, Acta Mater. 53 (2005) 2169-2179

[34] J.P. Couzinié, L. Lilensten, Y. Champion, G. Dirras, L. Perrière, I. Guillot, On the room temperature deformation mechanisms of a TiZrHfNbTa refractory high-entropy alloy, Mater. Sci. Eng. A, 645(2015) 255-263.

[35] Q. Wei, S. Cheng, K.T. Ramesh, E. Ma, Effect of nanocrystalline and ultrafine grain sizes on the strain rate sensitivity and activation volume: fcc versus bcc metals, Mater. Sci.Eng. A 381 (2004) 71-79.

[36] S.L. Yan, H. Yang, H.W. Li, X. Yao, Variation of strain rate sensitivity of an aluminum alloy in a wide strain rate range: Mechanism analysis and modeling, J. Alloy Compd 688 (2016) 776-786.

[37] Yoshinori Iwahashi, Zenji Horita, Minoru Nemoto, Terence G Langdon, The process of grain refinement in equal-channel angular pressing , Acta Mater 46 (1998) 3317-3331

[39] Yoshinori Iwahashi, JingtaoWang, Zenji Horita, Minoru Nemoto, Terence G. Langdon, Principle of equal-channel angular pressing for the processing of ultra-fine grained materials, Scripta Mater 35 (1996)143-146

[40] Y.W. Chen, Y.T Tsai, P.Y. Tung, S.P. Tsai, C.Y. Chen, S.H. Wang, J.R Yang, Phase quantification in low carbon Nb-Mo bearing steel by electron backscatter diffraction technique coupled with kernel average misorientation, Mater Charact 139 (2018) 49-58.

[41] Y.W. Chen, B.M. Huang, Y.T. Tsai, S.P. Tsai, C.Y. Chen, J.R. Yang, Microstructural evolutions of low carbon Nb/Mo-containing bainitic steels during high-temperature tempering, Mater Charact 131 (2017) 298–305.

[42] B.M. Huang, J.R. Yang, H.W. Yen, C.H. Hsu, C.Y. Huang, H. Mohrbacher, Secondary hardened bainite, Mater. Sci. Technol. 30 (2014) 1014–1023.

[43] S. Zaefferer, P. Romano, F. Friedel, EBSD as a tool to identify and quantify bainite and ferrite in low-alloyed Al-TRIP steels, J. Microsc. 230 (2008) 499–508.

[44]S.L. Shrestha, A.J. Breen, P. Trimby, G. Proust, S.P. Ringer, J.M. Cairney, An automated method of quantifying ferrite microstructures using electron backscatter diffraction (EBSD) data, Ultramicroscopy 137 (2014) 40–47.

[45] S.I. Wright, M.M. Nowell, EBSD image quality mapping, Microsc.Microanal. 12 (2005) 72–84.

[46] B. Su, H.P. Lin, J.C. Kuo, Y.T. Pan, EBSD investigation on microstructure transformation in low carbon steel during continuous cooling, Can. Metall. Quart. 53 (2014) 352–361.

[47] D.P. Field, K.R. Magid, I.N. Mastorakos, J.N. Florando, D.H. Lassil and J.W. Morris Jr., Mesoscale strain measurement in deformed crystals: A comparison of X-ray microdiffraction with electron backscatter diffraction, Phil. Mag 90 (2010), 1451‑1464

[48] J.A. Venables and C.J. Harland, Electron back-scattering patterns—A new technique for obtaining crystallographic information in the scanning electron microscope, Phil. Mag. 27 (1973) 1193-1200.

[49] Etienne Brodu, Emmanuel Bouzy, Depth Resolution Dependence on Sample Thickness and Incident Energy in On-Axis Transmission Kikuchi Diffraction in Scanning Electron Microscope (SEM), Microsc. Microanal 23 (2017) 1096 - 1106

[50] S.X. Ren, E.A. Kenik, K.B. Alexander and A. Goyal, Exploring spatial resolution in electron back-scattered diffraction experiments via Monte Carlo simulation, Microsc. Microanal. 4 (1998) 15-22

[51] A. Winkelmann, Principles of depth-resolved Kikuchi pattern simulation for electron backscatter diffraction, Microsc 239 (2010) 32–45.